

The XMM-Newton view of three X-ray weak quasars: Iron emission and strong ionized absorption

N. Schartel¹, P. M. Rodríguez-Pascual¹, M. Santos-Lleó¹, J. Clavel², M. Guainazzi¹,
E. Jiménez-Bailón¹, and E. Piconcelli¹

¹ XMM-Newton Science Operations Centre, ESA, RSSD, ESAC, Apartado 50727, 28020 Madrid, Spain
e-mail: Norbert.Schartel@sciops.esa.int

² Astrophysics Mission Division, ESA, SCT-SA, ESTEC, Postbus 299, 2200 AG - Noordwijk, The Netherlands

Received 5 August 2004 / Accepted 17 November 2004

Abstract. We present the analysis of XMM-Newton observations of three X-ray weak quasars: PG 1001+054, PG 1535+547 and PG 2112+059. All objects are absorbed by ionized material showing high column densities, $N_{\text{H}} = 2.9 \times 10^{22} \text{ cm}^{-2}$ to $N_{\text{H}} = 1.9 \times 10^{23} \text{ cm}^{-2}$, and ionization parameters, $\xi = 147 \text{ erg cm s}^{-1}$ to $\xi = 542 \text{ erg cm s}^{-1}$. The spectra of PG 1535+547 require an additional partial covering by neutral material with a column density of $N_{\text{H}} \approx 9 \times 10^{22} \text{ cm}^{-2}$ at a covering factor of ≈ 0.96 .

The spectra of PG 1535+547 show systematic residuals in the energy range from $\sim 4 \text{ keV}$ to $\sim 6 \text{ keV}$, which are inconsistent with K_{α} -fluorescence-emission of neutral or ionized iron under the assumption of a Gaussian line profile. They can be described with a relativistic disk line (*Laor*) and establish therefore the second X-ray weak quasar with such a spectral characteristic.

Our results together with the findings of Brinkmann et al. (2004, A&A, 414, 107) and Piconcelli et al. (2004a, MNRAS, 351, 161), indicate that warm absorbers characterized by high column densities and ionization parameters are typical of X-ray weak quasars. The occurrence of a variable relativistic broad Fe K_{α} fluorescence line in two out of the five well studied X-ray weak quasars might indicate a second general characteristic of the entire object class.

Based on observations obtained with XMM-Newton, an ESA science mission with instruments and contributions directly funded by ESA Member States and NASA.

Key words. X-ray: galaxies – quasars: individual: PG 1001+054 – quasars: individual: PG 1535+547 – quasars: individual: PG 2112+059

1. Introduction

The average dependency of the ratio of X-ray luminosity to optical luminosity as a function of redshift and optical luminosity for quasars was established by Avni & Tananbaum (1982). About two years later it was becoming evident that the ratio of X-ray to optical luminosity can be very low, e.g. PKS 1004+13 (Elvis & Fabbiano 1984). In 1997 the population of such quasars could be better constrained as it was discovered that the X-ray emission in about 10% of quasars is fainter, by a factor 10–30, than expected on the basis of their luminosity at other wavelengths. These quasars form a distinct class, and are called “X-ray weak” or “soft X-ray weak” quasars.

The population of X-ray weak quasars was constrained by Laor et al. (1997) based on ROSAT observations of a complete sub-sample of the Bright Quasar Survey (Green 1976; Schmidt & Green 1983), characterized by low redshift, $z \leq 0.4$, and low Galactic equivalent column density, $N_{\text{H}} < 1.9 \times 10^{20} \text{ cm}^{-2}$. Three out of the 23 studied quasars showed an X-ray flux which was significantly lower, by a factor 10–30, than expected on the basis of their emission at other

wavelengths. A bimodal distribution of the X-ray luminosity with respect to optical measurements was also found in a sample of AGNs studied by Wang et al. (1996), where 6 out of the 86 analyzed AGN show an $\alpha_{\text{OX}} < -2$ (Laor et al. 1997). As the ROSAT spectra of X-ray weak quasars do not show a distinctive spectral slope, Laor et al. (1997) discussed two possible scenarios for the origin of their X-ray weakness: either that for unknown reasons the X-ray emission mechanism of quasars is intrinsically bimodal or that the direct X-ray flux is obscured and only scattered X-ray flux can be observed. In this context, it is interesting to note that X-ray absorption by partially ionized gas (“warm absorber”) was detected in only $\sim 5\%$ of the whole population in the Laor sample in sharp contrast with lower luminosity AGNs, where it is much more frequent ($\sim 50\%$ Reynolds 1997). Recent studies (Porquet et al. 2004; Piconcelli et al. 2004b) indicate that the fraction of quasars showing warm absorber is comparable with the fraction found for lower luminosity AGNs.

Based on archival ROSAT, ASCA and *Einstein* observations of the 87 quasars in the Boroson & Green (1992) sample, Brandt et al. (2000) searched systematically for X-ray weak quasars. They found that the distribution of α_{OX} provides a

Table 1. PG-name, redshift and Galactic column density. The redshifts are taken from Véron-Cetty & Véron (2000).

Target	z	$N_{\text{H Gal.}}$ [10^{20} cm^{-2}]
PG 1001+054	0.161	1.88 (Elvis et al. 1998)
PG 2112+059	0.457	6.26 (Lockman & Savage 1995)
PG 1535+547	0.038	1.35 (Murphy et al. 1996)

clear separation between X-ray weak and “normal” quasars, where the former ones fulfill $\alpha_{\text{OX}} \leq -2$, which holds for $\sim 11\%$ of the entire sample. X-ray weak quasars show a strong correlation between α_{OX} and the C IV absorption equivalent width, which suggests that absorption is the primary cause of their soft X-ray-weakness. This correlation reveals a continuum of absorption properties connecting unabsorbed quasars, X-ray warm absorber quasars, soft X-ray weak quasars and Broad Absorption Line (BAL) quasars. However, soft X-ray weak quasars exhibit distinctive properties. They are characterized by low [O III] luminosity and equivalent widths. Most of them are located toward the weak [O III] end of the Boroson & Green eigenvector 1, likewise many BAL quasars. As it has been suggested for AGN with similar eigenvectors, it is possible that X-ray weak quasars are characterized by extreme physical parameters in the nuclear region, like a high mass accretion rate relative to the Eddington limit ($\dot{M}/\dot{M}_{\text{Edd}}$).

We report here on XMM-Newton observations of three X-ray weak quasars performed in 2002 and 2003 (Table 1). These observations together with our approved observing program for 2004, observations performed in the guaranteed program of XMM-Newton and an observing program of Brinkmann et al. (2004), will provide XMM-Newton observations of the entire sample of X-ray weak quasars established by Brandt et al. (2000).

The paper is organized as follows. In Sect. 2 we describe optical characteristics and previous X-ray studies of the three quasars. The XMM-Newton observations and their data reduction are described in Sect. 3. In Sect. 4 the X-ray spectral analysis of each quasar is provided. The spectral energy distribution is discussed in Sect. 5. Finally, in Sect. 6 we compare our findings with the previous results and infer some constraints on the regime of soft X-ray weak quasars from our results.

2. Optical and previous X-ray studies

2.1. PG 1001+054

The $H\beta$ emission of PG 1001+054 shows a $FWHM_{H\beta} = 1740 \text{ km s}^{-1}$, which classifies the source as a narrow line quasar (NLQ), for which $FWHM_{H\beta} < 2000 \text{ km s}^{-1}$ (Wills et al. 2000). In addition the ultraviolet spectrum is characterized by broad CIV and Ly α absorption, which in addition classifies PG 1001+054 as a broad absorption line (BAL) quasar (Brandt et al. 2000; Wills et al. 2000; Wang et al. 2000).

The quasar has the lowest α_{OX} value in the sample studied by Wang et al. (1996) and in the sample studied by Laor et al. (1997). Based on a comparison between the ROSAT X-ray observations and the UV absorption and emission lines,

Wang et al. (2000) concluded that the observed UV line depth is much lower than expected from the X-ray absorbing column density.

2.2. PG 2112+059

The HST spectrum of this quasar reveals broad absorption lines which classify PG 2112+059 as BAL quasar (Jannuzi et al. 1998). The low α_{OX} value, which defines PG 2112+059 as a X-ray weak quasar was already reported by Wang et al. (1996).

PG 2112+059 was detected with ROSAT which is generally unusual for BAL quasars (Green & Mathur 1996). The number of counts accumulated during the ROSAT observations was enough to allow an estimate of the absorbing column density of $1.5 \times 10^{21} \text{ cm}^{-2}$, for $\Gamma = 2.2$ (Wang et al. 1996).

An ASCA observation from October 1999 measured a photon index of $\Gamma = 1.44$ if absorption was fixed at the Galactic equivalent column density (Gallagher et al. 2001), which is rather flat for a typical quasar. In addition the fit was rather poor, i.e. it could be rejected at a 96% confidence level. From the statistical point of view the data can equally well be described with a power law absorbed by neutral material, partial covering or with an ionization edge (Gallagher et al. 2001). A comparison between the low energy ASCA data ($< 1 \text{ keV}$) with an extrapolated power-law model that was fitted on the spectrum above 2 keV shows that the spectrum recovers toward the lowest energy bins. As neutral cold absorption would depress all flux below $\approx 3 \text{ keV}$, the comparison speaks against a cold neutral absorber favoring either partial covering or ionized absorption. Comparing the ASCA observation with ROSAT data Gallagher et al. (2004) found flux variability of almost a factor of four.

An even larger flux and spectral variability was found with respect to the Chandra observation of PG 2112+059 from September 2002 (Gallagher et al. 2004), where the continuum was a factor ~ 3.5 lower than in the ASCA observation. The Chandra spectrum can be modeled by a power law folded by a warm absorber as well as by a power law folded by partially covering neutral absorption with equal statistical significance. The spectral variability was interpreted as evidence for an increase of the absorbing column density by Gallagher et al. (2004), as the two observations cannot be modeled with an absorber of constant column density. The Chandra data statistically require a broad iron K_{α} fluorescence emission line, in contrast to the 1999 ASCA data where the line could be excluded at a very high confidence level.

2.3. PG 1535+547 (Mrk 486, I Zw 121)

PG 1535+547 shows a narrow Balmer line with $FWHM = 1480 \text{ km s}^{-1}$ and therefore satisfies the criterion to be a NLQ (Véron-Cetty et al. 2001; Boroson & Green 1992). The optical Fe II emission is relatively strong (Phillips 1978), which supports the quasar’s classification as the optical Fe II emission in general anti-correlates with the Balmer line $FWHM$.

Table 2. Exposure details: (1) observation ID; (2) exposure number used in Table 3.

Target	Obs. ID ⁽¹⁾	Exp. No. ⁽²⁾	Camera	Start date and time [UT]	End date and time [UT]
PG 1001+054	0150610101	1	pn	2003-05-04 at 14:51:02	2003-05-04 at 17:45:52
		2	MOS 1	2003-05-04 at 14:27:34	2003-05-04 at 17:45:32
		3	MOS 2	2003-05-04 at 14:27:34	2003-05-04 at 17:45:37
		4	OM	2003-05-04 at 11:16:53	(exposure time: 5000 s)
		5	OM	2003-05-04 at 12:45:20	(exposure time: 3000 s)
PG 2112+059	0150610201	6	pn	2003-05-14 at 15:33:10	2003-05-14 at 19:51:46
		7	MOS 1	2003-05-14 at 15:10:39	2003-05-14 at 19:51:26
		8	MOS 2	2003-05-14 at 15:10:39	2003-05-14 at 19:51:31
		9	OM	2003-05-14 at 15:15:17	(exposure time: 5000 s)
PG 1535+547	0150610301	10	pn	2002-11-03 at 01:28:48	2002-11-03 at 09:20:44
		11	MOS 1	2002-11-03 at 01:06:17	2002-11-03 at 09:20:24
		12	MOS 2	2002-11-03 at 01:06:17	2002-11-03 at 09:20:24

PG 1535+547 is the X-ray weakest quasar detected in the Boroson & Green (1992) AGN sample by Brandt et al. (2000).

A power law fit to the ASCA spectrum with absorption fixed at the Galactic value plus an additional intrinsic absorption component resulted in a photon index of $\Gamma = 0.44$, which is abnormally flat for a typical type 1 AGN (Gallagher et al. 2001). A statistically better fit was obtained by the same authors with a partial covering model. The best fit model parameters were: an intrinsic neutral absorption column density of $1.23^{+0.83}_{-0.54} \times 10^{23} \text{ cm}^{-2}$ with covering factor of $0.91^{+0.07}_{-0.26}$ and $\Gamma = 2.02^{+0.92}_{-0.95}$. For comparison, a fit with an ionized absorber left clear systematic residuals and was characterized by $\Delta\chi^2 = +17$ for the same number of degrees of freedom.

3. Observations and data reduction

The exposures discussed in this article were taken with the European Photon Imaging Camera (EPIC) and with the Optical Monitor (OM) on board of XMM-Newton (Jansen et al. 2001). Unfortunately, the sources are too weak to be detected with the Reflection Grating Spectrograph, RGS. All OM exposures discussed in the following were performed with the visible gratings in the light path of OM (Mason et al. 2001). OM exposures of PG 1535+547 were precluded because of the presence of a star brighter than 6th magnitude in the field of view. The EPIC consists of three simultaneously working cameras: the pn-camera (Strüder et al. 2001) and two MOS-cameras (Turner et al. 2001). Consequently three spectra are measured simultaneously during each observation. All EPIC exposures were taken in the Full Frame mode with the optical thin blocking filter. The observation details are provided in Table 2.

We used the standard Science Analysis System (SAS) v.5.4.1 (linux version, Loiseau 2004), and recent calibration files (November/December 2003) for the processing and extraction of the data.

The OM observations were processed with the OMICHAIN routine of SAS which applied the required astrometric and photometric corrections. The raw pn and MOS data were processed with the EPCHAIN and EMCHAIN tasks provided by SAS in

order to generate the relative linearized event files. For pn only events with patterns 0–4, which characterize single and double events, were selected. For MOS events with patterns 0–12 were chosen, which correspond to single, double, triple and quadruple events. The applied pattern selection ensures a good energy calibration, and allows the usage of standard detector response and effective area calculation.

The screening for time ranges with low radiation background level was done following the method described by Piconcelli et al. (2004a). The source extraction area, the energy range used for the screening and the corresponding rejection thresholds, the background extraction area, the net count rate for the source and the finally utilized accumulated exposure times for each exposure are shown in Table 3.

All source events were extracted within a circular region centered at the peak of the emission, which was determined by eye. The details are provided in Table 3. The background was determined from source-free regions nearby the source. For all MOS exposures the background was determined from an annulus around the extraction area of the source counts, whereas an offset circular region was chosen for the pn background extraction. The background for each exposure was determined from counts collected at the same CCD in order to minimize calibration uncertainties. In addition the center of the circular background extraction region of the pn data was selected to have similar CCD y -coordinates which minimizes the charge transfer efficiency dependency on the detector coordinates. The locations are specified in the Table 3.

The detector response and the effective area were generated with the SAS tasks RMFGEN and ARFGEN, respectively.

4. X-ray spectral analysis

Following the current calibration recommendation (Kirsch 2003), we restricted the analysis of the MOS spectra to the energy range from 0.5 keV to 10.0 keV and of pn spectra to the 0.3 to 12.0 keV energy range, respectively. Due to the low source count rates found in the MOS observations, we added

Table 3. Source extraction and low background screening process: (1) an annulus with an inner radius of 1' and an outer radius 5' centered on the source position was used as reference area for the screening. The data were binned with 10 s; (2) coordinates in J2000; (3) extraction radius for the source; (4) energy range considered for the screening; (5) rejection threshold for screening; (6) for annular background areas the inner and the outer radius are provided. (7) background corrected count rate in the energy range of 0.3–12.0 keV for pn and 0.5–10.0 keV for MOS, respectively; (8) accumulated exposure time.

Exp. Nr.	Source extraction			Screening ⁽¹⁾		Background extraction			Net source	
	RA ⁽²⁾ [h:m:s]	Dec ⁽²⁾ [d:m:s]	$r^{(3)}$ [']	Energy ⁽⁴⁾ [keV]	CR ⁽⁵⁾ [s ⁻¹]	RA ⁽²⁾ [h:m:s]	Dec ⁽²⁾ [d:m:s]	$r^{(6)}$ [']	CR ⁽⁷⁾ [10 ⁻² s ⁻¹]	$T^{(8)}$ [s]
1	10:04:20.29	+05:12:59.6	0.30	0.3–12.0	2.0	10:04:14.47	+05:13:22.1	0.6	3.57 ± 0.21	8815
2	10:04:20.33	+05:12:58.6	0.30	0.5–10.0	0.5	Source	Source	1.0–2.0	0.71 ± 0.08	10 966
3	10:04:20.29	+05:12:59.6	0.30	0.5–10.0	0.5	Source	Source	1.0–2.0	0.53 ± 0.07	11 009
6	21:14:52.45	+06:07:41.6	0.30	0.3–12.0	10.	21:14:57.25	+06:08:06.6	0.6	11.1 ± 0.34	10 507
7	21:14:52.42	+06:07:40.7	0.30	0.5–10.0	2.0	Source	Source	1.0–2.5	3.25 ± 0.16	13 287
8	21:14:52.58	+06:07:40.7	0.30	0.5–10.0	2.0	Source	Source	1.0–2.5	2.99 ± 0.15	13 248
10	15:36:38.43	+54:33:32.3	0.35	0.3–12.0	7.0	15:36:36.14	+54:32:27.3	0.6	14.2 ± 0.29	20 031
11	15:36:38.37	+54:33:31.8	0.30	0.5–10.0	3.0	Source	Source	0.8–1.4	4.01 ± 0.13	26 523
12	15:36:38.31	+54:33:32.9	0.30	0.5–10.0	3.0	Source	Source	0.8–1.4	4.03 ± 0.13	26 516

the MOS1 and MOS2 spectra of each source and determined the corresponding mean detector response and auxiliary files.

The source spectra were binned to ensure a constant signal-to-noise ratio for each bin, restricting to a maximum of three bins per energy resolution element. With this choice for the binning over-sampling is avoided and the Gaussian distribution is approximately reached which authorizes the use of χ^2 statistics. The spectral analysis was performed with XSPEC 11.2.0 (linux version, Arnaud 1996). For the estimates of the spectral parameters the modified minimum χ^2 method is used (Kendall & Stuart 1973), which requires the applied binning with constant signal-to-noise in order to avoid biasing effects due to the intrinsic correlation between the accumulated counts and their error. The errors of estimated parameters are given for the 90% confidence region for a single interesting parameter ($\chi^2 = 2.7$, Avni 1976).

The various absorption components were modeled assuming cosmic abundances according to Anders & Grevesse (1989), and photoelectric absorption cross sections as provided by Balucinska-Church & McCammon (1992), with the exception for helium, for which the cross sections were taken from Yan et al. (1998).

All fits were performed assuming Galactic foreground absorption. The Galactic column densities were fixed at the values inferred from 21 cm observations. They are provided in Table 1 together with the reference to the corresponding publications. The intrinsic absorption was always fitted with the redshift fixed at the value of the source as provided in Table 1.

4.1. PG 1001+054

The spectra of PG 1001+054 have the lowest signal-to-noise ratio of the three observations. Both the pn and MOS spectra were binned with a signal-to-noise ratio of five under the binning constraints which are described above. The spectra

provide only 9 energy bins for pn and three for the co-added MOS spectra, which limits the statistical analysis.

For a neutral absorber, an absorbed power-law model and a partially covered source model can both be excluded from the resulting poor χ^2 statistics of 156.7 (d.o.f. = 9) and 71.1 (d.o.f. = 8), respectively. We fitted the absorption through ionized material as represented by the XSPEC model *absori* (Done et al. 1992). For this fit we forced the *absori* photon index to be equal to the (free) continuum power law index. The temperature of the absorbing material was fixed at $T = 3.0 \times 10^4$ K and its redshift was fixed at the redshift of the source. In addition the iron abundance was pegged to the value in Anders & Grevesse (1989), as described above. This fit of a power law absorbed by ionized material, i.e. a warm absorber, lead to an improvement of $\Delta\chi^2 = 55.5$ with respect to the partial covering model and provides an acceptable parameterization of the spectra. Despite the relative large $\chi^2 = 15.6$ (d.o.f. = 8), the low signal to noise ratio of the data does not warrant a more complex model. The estimated parameters and the statistical results are provided in Table 4. Contour plots of column density versus ionization parameter are given in Fig. 1.

4.2. PG 2112+059

The pn and the co-added MOS spectra were binned with a signal-to-noise ratio of 6, which provides 45 channels in total.

The values of χ^2 and the degrees of freedom for all fits are provided in Table 4. A power law model absorbed by intrinsic neutral material can be ruled out ($\chi^2 = 92.0$ and d.o.f. = 41). Although a partial covering model decreases the value of χ^2 , it can still be ruled out at the 99% confidence. The existence of systematic residuals also argue strongly against both models.

The X-ray spectra can be well described by a power law absorbed by ionized material. The choice of fixed and free parameters was the same as for PG 1001+054. The best fit

Table 4. Spectral fits of the EPIC spectra of the quasars. The errors for the 90% confidence level are provided if $\chi^2_{\text{reduced}} < 2.0$. Fits labeled with \ddagger have $\chi^2_{\text{reduced}} > 2.0$ and consequently no errors were determined. Fits labeled with \dagger were performed over the 2–10 keV energy range for MOS and the 2–12 keV energy range of pn, respectively. Explanation of labels: (1) explanation of the used models: *pl*: power-law (XSPEC: pow), *nab*: neutral absorber at the redshift of the source (XSPEC: zphabs), *pab*: partial covering with neutral absorber at the redshift of the source (XSPEC: zpcfabs), *iab*: ionized absorption at the redshift of the source (XSPEC: absori), *ga*: Gaussian line at the redshift of the source (XSPEC: zgauss), *la*: relativistic disk line after Laor (XSPEC: laor, Laor et al. 1997); Parameters: (a) equivalent column density; (b) covering fraction; (c) ionization level of absorbing material $\xi = L/nr^2$, as defined in *XSPEC*; (d) photon flux at 1 keV; (e) degrees of freedom.

Fit model ⁽¹⁾	Absorber				Continuum		Statistic	
	neutral $N_{\text{H}}^{(a)}$ [10^{22} cm^{-2}]	$cf^{(b)}$	warm $N_{\text{H}}^{(a)}$ [10^{22} cm^{-2}]	$\xi^{(c)}$ [erg cm s^{-1}]	Γ	power-law $N^{(d)}$ [$\text{keV}^{-1} \text{ cm}^{-2} \text{ s}^{-1}$]	χ^2	$d^{(e)}$
<u>PG 1001+054</u>								
1 <i>nab * pl</i>	0.00 \ddagger				3.77 \ddagger	$1.02^{\ddagger} \times 10^{-5}$	156.7	9
2 <i>pab * pl</i>	7.86 \ddagger	0.95 \ddagger			3.20 \ddagger	$2.44^{\ddagger} \times 10^{-4}$	71.1	8
3 <i>iab * pl</i>			$19.2^{+11.9}_{-7.3}$	542^{+97}_{-147}	$1.97^{+0.17}_{-0.14}$	$6.62^{+1.01}_{-0.71} \times 10^{-5}$	15.6	8
<u>PG 2112+059</u>								
4 <i>nab * pl</i>	0.00 \ddagger				1.54 \ddagger	$7.40^{\ddagger} \times 10^{-5}$	92.0	41
5 <i>pab * pl</i>	$4.55^{+1.55}_{-1.17}$	$0.69^{+0.08}_{-0.12}$			$2.17^{+0.09}_{-0.20}$	$2.02^{+0.62}_{-0.53} \times 10^{-4}$	65.1	40
6 <i>iab * pl</i>			$3.53^{+1.33}_{-0.96}$	270^{+125}_{-72}	$1.92^{+0.09}_{-0.09}$	$1.35^{+0.14}_{-0.13} \times 10^{-4}$	38.7	40
<u>PG 1535+547</u>								
7 <i>nab * pl</i>	6.94 \ddagger				1.67 \ddagger	$5.18^{\ddagger} \times 10^{-4}$	807.3	108
8 <i>pab * pl</i>	8.16 \ddagger	0.95 \ddagger			1.53 \ddagger	$4.17^{\ddagger} \times 10^{-4}$	357.5	107
9 <i>iab * pl</i>			12.71^{\ddagger}	533^{\ddagger}	1.03 \ddagger	$1.57^{\ddagger} \times 10^{-4}$	338.2	107
10 <i>pab * iab * pl</i>	$10.3^{+0.8}_{-0.8}$	$0.97^{+0.01}_{-0.02}$	$2.41^{+0.86}_{-0.57}$	136^{+81}_{-50}	$2.13^{+0.05}_{-0.05}$	$1.37^{+0.14}_{-0.13} \times 10^{-3}$	132.8	105
11 <i>iab * (pl + la)</i>			$12.2^{+0.5}_{-0.7}$	528^{+84}_{-24}	$1.08^{+0.01}_{-0.04}$	$1.29^{+0.06}_{-0.03} \times 10^{-4}$	157.8	103
12 <i>pab * iab * (pl + ga)</i>	$9.72^{+0.60}_{-0.50}$	$0.97^{+0.01}_{-0.01}$	$2.52^{+0.27}_{-0.25}$	145^{+23}_{-19}	$2.13^{+0.04}_{-0.05}$	$1.28^{+0.04}_{-0.04} \times 10^{-3}$	115.8	102
13 \dagger <i>pab * iab * (pl + ga)</i>	$13.2^{+1.0}_{-1.3}$	$0.92^{+0.01}_{-0.01}$	$9.78^{+1.09}_{-1.38}$	2126^{+1379}_{-698}	$2.65^{+0.16}_{-0.18}$	$3.87^{+0.13}_{-0.19} \times 10^{-3}$	87.5	81
14 <i>pab * iab * (pl + la)</i>	$8.90^{+0.57}_{-0.56}$	$0.96^{+0.01}_{-0.01}$	$2.91^{+0.81}_{-0.57}$	147^{+70}_{-48}	$2.05^{+0.04}_{-0.05}$	$1.03^{+0.09}_{-0.10} \times 10^{-3}$	104.1	101
15 \dagger <i>pab * iab * (pl + la)</i>	$10.6^{+1.8}_{-1.3}$	$0.93^{+0.02}_{-0.03}$	$6.60^{+3.71}_{-2.90}$	620^{+1087}_{-490}	$2.32^{+0.20}_{-0.19}$	$1.89^{+0.22}_{-0.30} \times 10^{-3}$	83.4	80

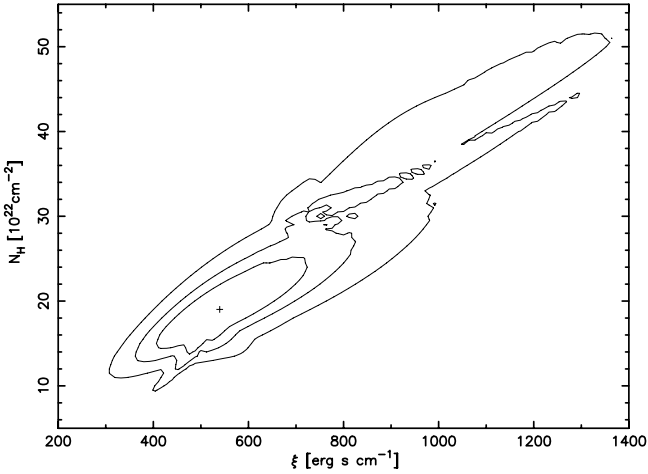


Fig. 1. PG 1001+054: the confidence levels to 68.3%, 90% and 99% for two interesting parameters: column density and ionization parameter are shown.

parameters are provided in Table 4. The significance contours for the absorbing column density versus the ionization parameter are shown in Fig. 2.

In order to allow an investigation of the variability with respect to previous Chandra and ASCA observations

(Gallagher et al. 2004) we determined the flux for the energy bands 0.5–2.0 keV and 2.0–7.0 keV to be $1.74^{+0.12}_{-0.45} \times 10^{-13} \text{ erg cm}^{-2} \text{ s}^{-1}$ and $2.75^{+0.21}_{-0.50} \times 10^{-13} \text{ erg cm}^{-2} \text{ s}^{-1}$, respectively. The spectra of the XMM-Newton observation do not show residuals around the energy range of the Fe K_{α} fluorescence emission line. But it has to be considered that the individual energy bins cover a wide energy range due to the low statistics at higher energies. Therefore, we added a redshifted Gaussian emission line with centroid energy and width fixed at the values found by Gallagher et al. (2004): $E_C = 6.38 \text{ keV}$ and $\sigma = 0.46 \text{ keV}$. The resulting fit leads to an improvement of $\Delta\chi^2 = 5.01$ corresponding to an F-statistics probability of 97.91% and as such does not allow to claim a detection of the line. The best fitted line emissivity, is $I_L = 6.8^{+4.8}_{-4.9} \times 10^{-6} \text{ photons cm}^{-2} \text{ s}^{-1}$ corresponding to an equivalent width, $EW = 0.67^{+0.58}_{-0.50} \text{ keV}$.

4.3. PG 1535+547

The pn as well as the co-added MOS spectra were binned with a signal-to-noise ratio of 6, resulting in 112 channels in total.

A power law continuum absorbed by neutral material at the redshift of the source, a continuum absorbed by neutral material partially covering the source, as well as a continuum absorbed by ionized material can be excluded according

Table 5. Spectral fits of the emission line of PG 1535+547. The corresponding continuum fits are provided in Table 4. Fits labeled with † were performed over the 2–10 keV energy range for MOS and the 2–12 keV energy range of pn, respectively. (1) The following two models are used: *ga*: Gaussian line at redshift of source (XSPEC: zgauss), *la*: relativistic disk line after Laor (XSPEC: laor, Laor 1991); Parameters: (a) energy of line in rest frame of quasar; (b) line width (σ); (c) total photons in line; (d) inclination angle

Fit	Emission line model	Energy ^(a) [keV]	Width ^(b) [keV]	Norm ^(c) [cm ⁻² s ⁻¹]	<i>R</i> (in) [G M c ⁻²]	<i>R</i> (out) [G M c ⁻²]	Inclination ^(d) [degree]
11	la	6.4 (fixed)		5.38 ^{+0.49} _{-0.68} 10 ⁻⁵	1.77 ^{+0.22} _{-0.77}	7.83 ^{+1.40} _{-0.66}	31.85 ^{+2.40} _{-1.45}
12	ga	6.00 ^{+0.14} _{-0.21}	0.26 ^{+0.21} _{-0.11}	7.16 ^{+2.69} _{-2.70} 10 ⁻⁶			
13 [†]	ga	6.06 ^{+0.14} _{-0.14}	0.19 ^{+0.14} _{-0.08}	5.22 ^{+3.16} _{-2.71} 10 ⁻⁶			
14	la	6.4 (fixed)		1.63 ^{+0.42} _{-0.42} 10 ⁻⁵	5.67 ^{+2.16} _{-1.32}	9.47 ^{+1.59} _{-2.08}	28.38 ^{+4.36} _{-2.28}
15 [†]	la	6.4 (fixed)		1.28 ^{+0.49} _{-0.44} 10 ⁻⁵	7.00 ^{+0.96} _{-2.57}	8.16 ^{+3.06} _{-0.75}	28.63 ^{+4.43} _{-2.18}

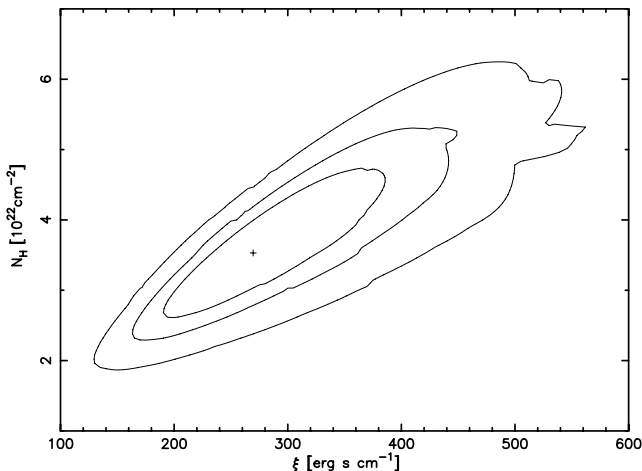


Fig. 2. PG 2112+059: the confidence levels to 68.3%, 90% and 99% for two interesting parameters: column density and ionization parameter are shown.

to the obtained χ^2 values with respect to the degrees of freedom. The choice of fixed and free parameters was the same as for PG 1001+054. The best fit parameters, the corresponding χ^2 -values and degrees of freedom are provided in Table 4.

A model assuming a continuum absorbed by ionized material and partially covered by a neutral absorber at the same time leads to a fit acceptable at the 95% confidence level (fit 10 in Table 4). The best-fit model, the data points and the resulting residuals are shown in Fig. 3. The large excess between 4 keV and 6 keV indicates the presence of a fluorescence iron emission line. Adding a red-shifted Gaussian emission line (XSPEC model zgauss) to the applied model improves the obtained χ^2 value by $\Delta\chi^2 = 17.0$. In Fig. 4 the 68.3%, 90% and 99% confidence level for two interesting parameters, line energy in the rest-frame of PG 1535+547 and line width, are shown. They indicate that the line is most probably broad and not well constrained toward lower energies. But most important is that a line energy of 6.4 keV, i.e. the energy of the neutral Fe K α fluorescence line, can be excluded at the 99.0% confidence level. Since ionization of iron shifts the transition toward higher energies, a Gaussian profile can be excluded for the iron K α line.

A satisfactory description of the data is provided if the fluorescence iron emission is described with a relativistically broadened line profile emitted in an accretion disk around a

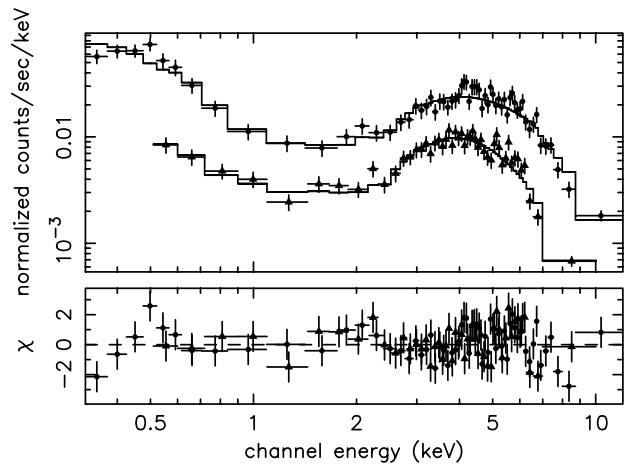


Fig. 3. PG 1535+547: the data compared with the best fitted model for a power law continuum absorbed by ionized material and partially covered by neutral material (pn: filled circles and MOS filled triangles). The best fit parameters are given in Table 4. Systematic residuals are appearing between 4 and 6 keV, i.e. the energy range of the fluorescence Fe K α line emission.

Kerr black hole (model *laor* in XSPEC, Laor 1991). The line energy was fixed at the energy of the neutral Fe K α transition, i.e. 6.4 keV in the rest frame of the quasar, which is 6.166 keV in the observed frame. The emissivity index β ($\epsilon \propto r^\beta$) was fixed at $\beta = 3$, whereas the inner and the outer radius, the inclination angle and the normalization were allowed to vary. The best fit model is plotted in Fig. 5, together with the data and the residuals. The model parameters are listed in Table 4. The resulting χ^2 improves by $\Delta\chi^2 = 28.7$ with respect to the model without emission line and by $\Delta\chi^2 = 11.7$ relative to the model with Gaussian profile, significant at the 99.99% and 99.89% level, respectively. As shown in Fig. 6 the column density of the warm absorber is correlated with the column density of the partially covering neutral material. For the ionized absorber the confidence levels of 68.3%, 90% and 99% for two interesting parameters, column density and ionization parameter, are shown in Fig. 7.

To investigate the nature of the central black hole we calculated confidence contours for the inner and the outer radius of the iron line emission area of the accretion disk. The 68.3%, 90% and 99% confidence level contours are shown in Fig. 8.

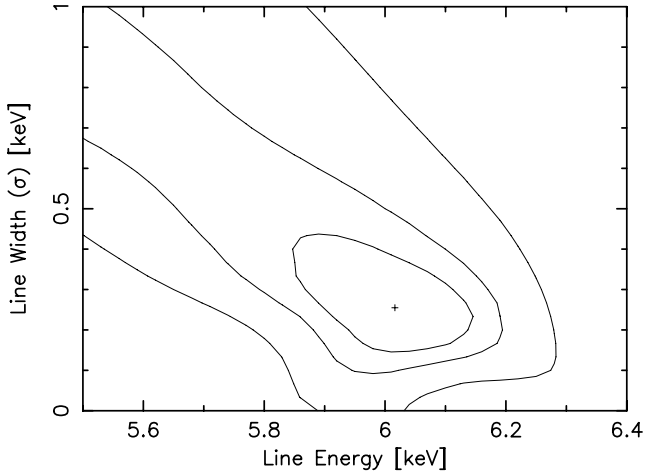


Fig. 4. PG 1535+547: the confidence levels to 68.3%, 90% and 99% for the two interesting parameters of a Gaussian line, line energy and line width, are shown. Both are in the rest-frame of PG 1535+547. The line energy is not compatible with an emission of neutral iron at 6.4 keV.

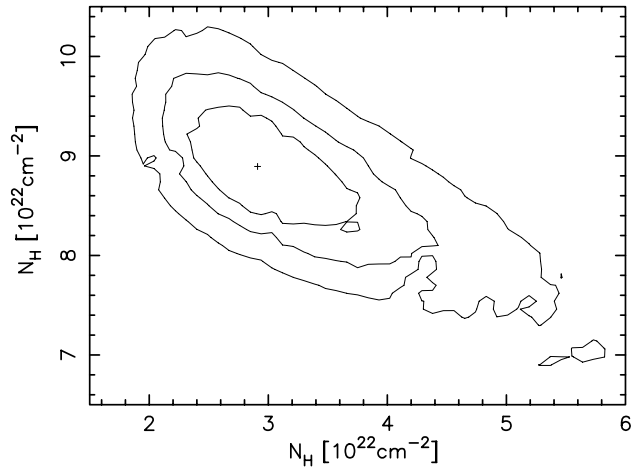


Fig. 6. PG 1535+547: the confidence levels to 68.3%, 90% and 99% for the two interesting parameters: column density of ionized absorber and column density of neutral absorber are shown.

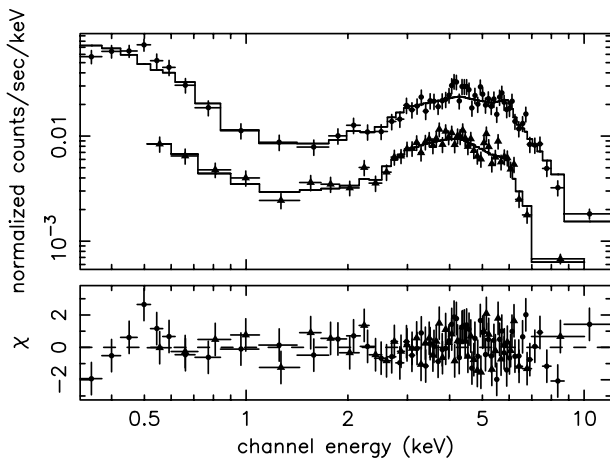


Fig. 5. PG 1535+547: the data compared with the best fitted model for a power-law continuum absorbed by ionized material and partially covered by neutral material. The fluorescence Fe K_{α} line is described by a relativistic disk line (XSPEC model *laor*, Laor 1991). MOS data are given by filled triangles and pn data by filled circles, respectively. The best fit parameters are given in Table 4 (fit 15).

Unfortunately, these results do not allow to distinguish between a non-rotating (Schwarzschild) and a rotating (Kerr) black hole.

Contrary to what is often found in quasars, the PG 1535+547 data do not require soft X-ray excess emission above the power law. The count rate is low below 2 keV and does not warrant such a complex model. It is important however to check that the relativistic iron K_{α} line is not an artifact resulting from an improper placement of the power law at low energies combined with the introduction of an ionized instead of a neutral absorber.

To test this hypothesis we repeated the fits described above but restricting the spectral analysis to the energy range above 2.0 keV. The best fit parameters are listed in Table 4 and fits are labeled with †. As expected, the statistical significance is lower than the significance obtained for the spectra covering

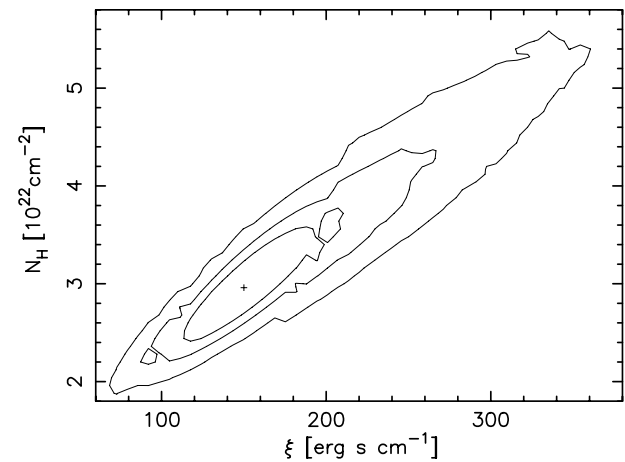


Fig. 7. PG 1535+547: the confidence levels to 68.3%, 90% and 99% for the two interesting parameters, column density of the ionized absorber and ionization parameter, are shown.

the whole energy range and even a description without Fe K_{α} fluorescence line emission becomes acceptable. However, the Gaussian line leads again to a line energy which is not in agreement with the redshift of PG 1535+547 and therefore must be excluded on the basis of physical arguments. Compared with the case without a line, the addition of a relativistic emission profile improves the fit by $\Delta\chi^2 = 14.3$, which is significant at the 98.8% confidence level.

5. Spectral energy distribution

PG 1001+054 was detected in the first visible grism exposure at an average flux of $(2.40 \pm 0.07) \times 10^{-15} \text{ erg cm}^{-2} \text{ s}^{-1} \text{ \AA}^{-1}$ in the 3500–4500 Å band and in the second exposure at an average flux of $(2.32 \pm 0.07) \times 10^{-15} \text{ erg cm}^{-2} \text{ s}^{-1} \text{ \AA}^{-1}$, respectively. In both UV grism observations the source could not be found. PG 2112+059 was observed with an average flux of $(3.52 \pm 0.08) \times 10^{-15} \text{ erg cm}^{-2} \text{ s}^{-1} \text{ \AA}^{-1}$ in the 3500–4500 Å band visible grism observation. Again, the source was not detected in the UV grism observations.

Both PG 1001+054 and PG 2112+059 had been observed with HST in the UV–optical domain. In order to have a snapshot of the optical-UV-X rays spectral energy distribution of these objects during their XMM-Newton observations we use the fluxes obtained with OM to scale the high resolution high S/N UV–optical spectra. The scaling factors are 1.4 for PG 1001+054 and 1.25 for PG 2112+059; the latter is more uncertain given the small wavelength overlap between HST and OM spectrum. The scaling factor used for PG 1001+054 corresponds to its brightness level in 1987 and 2002 and the scaling factor used for PG 2112+059 corresponds to its brightness level in 1993 and 1995, respectively. It is remarkable that OM reveals a relatively strong feature at ~ 4060 Å, consistent with MgII λ 2800 emission. As the quality of the HST spectra of PG 1535+547 is rather low, we have used its IUE spectrum instead.

Figure 9 shows the observed UV spectra of the three quasars. The similarity of the Galactic absorption features is remarkable in spite of the largely different HI column density in PG 1001+054 and PG 2112+059. The low resolution, low signal-to-noise ratio of the IUE spectrum of PG 1535+547 does not show clearly identifiable absorption features, except for galactic MgII.

In order to compare the intrinsic spectra of the three sources, the UV spectra were brought in the rest-frame of the quasars. In addition, the PG 2112+059 spectrum has been corrected for galactic reddening using the Cardelli et al. (1989) parametrization and assuming $E(B - V) = 0.15$. For the galactic reddening we have used the $NH/E(B - V)$ relation given by Dickey & Lockman (1990). After this correction, the overall UV spectral shapes of PG 1001+054 and PG 2112+059 are very similar, but PG 1535+547 shows an opposite trend: flux increasing with wavelength. A possibility to reverse the spectral shape of PG 1535+547 is to apply some reddening correction. However, the required color excess is too large for the galactic HI column density and for the absence of a significant 2200 Å feature (Smith et al. 1997). Therefore, if reddening is causing the atypical UV spectral shape in PG 1535+547, a galactic origin is very unlikely. In Fig. 10 and for the following analysis and modeling, we have applied the correction for the rest wavelength using the parametrization from Calzetti et al. (2000) with $E(B - V) = 0.35$. The applied intrinsic reddening was determined by iteration of the $E(B - V)$ value until the UV spectrum was becoming similar to the UV spectra of the other two quasars. This intrinsic reddening might be associated with the neutral absorbing material suggested by the X-rays data fits. If this is the case, then N_H/A_V ratio and, hence, the gas-to-dust ratio would be ~ 10 times larger than typical galactic values, as already found in other quasars (Alonso-Herrero et al. 2001). In their analysis of the polarization spectrum, Smith et al. (1997) conclude that dust is present in the BLR of this source, scattering/reddening the continuum and emission lines, but only partially; this result is in qualitative agreement with the partially covering neutral absorber found in the X-ray spectra.

The optical-UV-X-ray spectral energy distribution, SED, of the three sources is plotted in Fig. 11. Taking these SEDs into

account, we have run CLOUDY¹ models in order to match both the SED and the warm absorber parameters obtained from the X-ray spectral analysis. The incident continuum on the gas has been defined as

$$f_\nu = f_0 [\nu^{+\alpha_{UV}} \exp(-h\nu/kT_{\text{high}}) \exp(-kT_{\text{low}}/h\nu) + (\nu_{2 \text{ keV}}/\nu_{2500 \text{ \AA}})^{\alpha_{OX}} (\nu/\nu_{2 \text{ keV}})^{+\alpha_X}]$$

where the X-ray power law (second term) varies as $\nu^{5/2}$ at energies lower than ~ 1 eV and ν^{-2} at energies higher than ~ 50 keV.

The model parameters are listed in Table 6 and the results shown in Fig. 11. We remark that the model parameters are not the result of a fit to the SED; they have been chosen to match the results of the X-ray spectral analysis and tuned to give a reasonable representation of the SED. As can be seen in Table 6, the parameter α_{OX} of the intrinsic, incident continuum is well above the value -2.0 .

Our main purpose for running CLOUDY has been to investigate if the highly ionized gas should be expected to imprint line emission/absorption features into the spectrum. In the plot of the outward emission predicted by CLOUDY (Fig. 11) we have assumed rather narrow line profiles (500 km s^{-1}) which result in strongly peaked spectra. The purpose is to show that some emission features are indeed expected in the X-ray range, but no significant emission line is predicted in the UV.

According to the results of the CLOUDY models described here, it is rather difficult to get significant absorption features in the UV since the column densities of the ionic species producing UV absorptions are rather low (with the possible exceptions of NV λ 1240 Å and OVI λ 1033 Å): only for Ar and heavier elements a significant fraction of their atoms can retain more than 1–2 electrons.

6. Discussion

The discussion is divided in four parts. In the first one we discuss the X-ray absorption characteristics of the three X-ray weak quasars. The SED is discussed in the second part, the variability of PG 2112-059 in the third one and the Fe K α fluorescence emission line of PG 1535+547 is the subject of the fourth part.

6.1. Absorption in X-ray weak quasars

All three studied quasars are characterized by absorbers with high column densities and high ionization parameters. A neutral absorber in addition to the warm absorber is found only in the spectra of PG 1535+547. These findings are in agreement with the results obtained by Brinkmann et al. (2004) and Piconcelli et al. (2004a), who found strong absorption by ionized material in two X-ray weak quasars, namely PG 1411+442 and Mrk 304. The large effective area and improved spectral resolution of XMM-Newton for the first time allow to discriminate between competing absorption scenarios:

PG 1001+054: a neutral absorber as well as a partially covering neutral material can be excluded for our observation of PG 1001+054. The spectra can be described with

¹ We have used version C96b2; for details see www.nublado.org

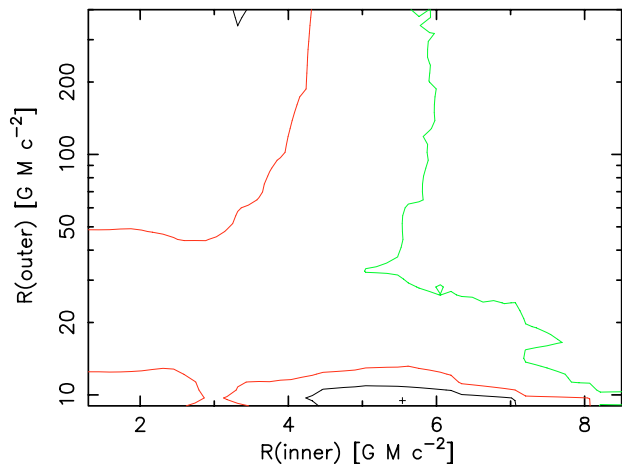


Fig. 8. PG 1535+547: confidence levels to 68.3% (green), 90% (red) and 99% (black) for the two interesting parameters: inner and outer radius, which characterize the area of the accretion disk emitting fluorescence Fe K_{α} line.

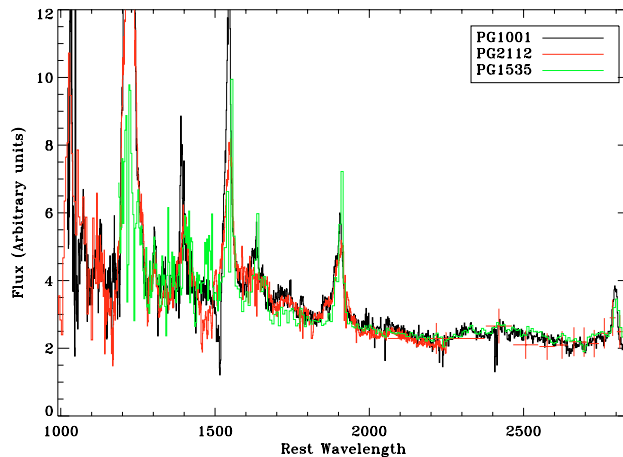


Fig. 10. Only when PG 2112+059 is corrected for reddening in our Galaxy and PG 1535+547 is corrected for intrinsic reddening the spectra at rest frame of the three objects become very similar.

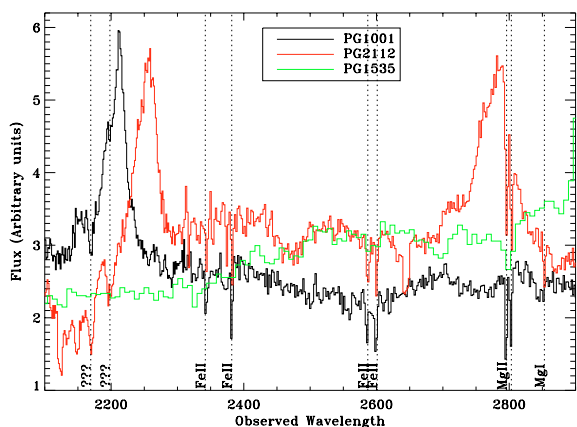


Fig. 9. The observed UV spectra of PG 1001+054, PG 2112+059 and PG 1535+547 show some common absorption features due to mildly ionized material in our Galaxy, but it is clear that the overall UV spectral shapes are widely different.

a warm absorber model. The high χ^2 value, with respect to the d.o.f., might indicate that a more complex model is required for a more satisfying description of the spectra. But due to the low number of collected photons it is not possible to introduce further components into the spectral model.

PG 2112+059: similar to PG 1001+054 a neutral absorber as well as partially covering with neutral material can be excluded for PG 2112+059, which was not possible in previous studies (Gallagher et al. 2001; Gallagher et al. 2004).

PG 1535+547: a description in terms of a neutral absorber, neutral partial covering or an ionized absorber can be excluded for the EPIC data of PG 1535+547. An acceptable description of the absorption properties can only be obtained through the combination of an ionized absorber and a neutral absorber with a large covering factor.

An ASCA observation from June 1999 could be described by either a warm absorber or a partial covering model; the latter allowing a slightly better statistical description of the data. Given the very large effective area of XMM-Newton

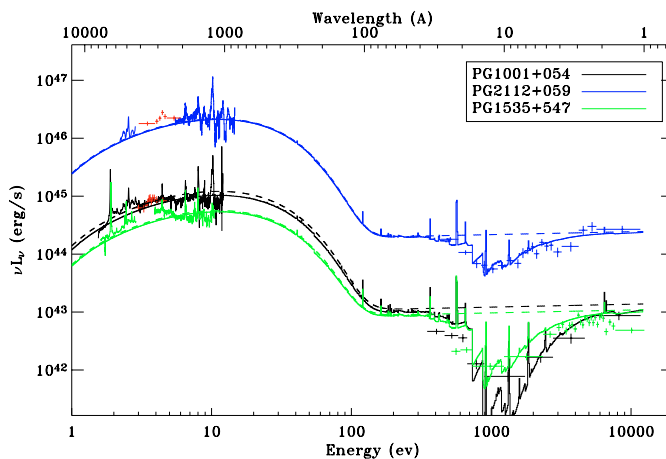


Fig. 11. Spectral energy distribution for PG 1001+054, PG 2112+059 and PG 1535+547. The OM observations (red error bars) have been used to re-scale UV spectra (IUE and HST) for PG 1001+054 and PG 2112+059. Unfortunately, for PG 1535+547 there are no OM data available to assure the proper scaling of the optical-UV-X-ray ranges. Optical-UV have been corrected for galactic reddening and X-ray corrected for galactic absorption. Input ionizing spectra in Cloudy models are drawn as dashed lines and output (transmitted and diffuse emission) as solid lines, both in the same color as object data.

in the soft X-ray region in comparison with ASCA and the fact that our description requires a partial covering of a neutral absorber in addition to a warm absorber, our results are in agreement with the findings of Gallagher et al. (2001).

Our results, in combination with the findings of Brinkmann et al. (2004) and Piconcelli et al. (2004a) indicate that all 5 X-ray weak quasars observed today are characterized by warm absorbers with high column densities and high ionization parameters. Although warm absorbers are common in lower luminosity AGNs, especially in Seyfert 1 nuclei (Reynolds 1997), their properties are quite different from those found here. More specifically, the Seyfert 1 absorbers have much lower column densities and ionization parameters than the X-ray weak quasars absorbers. A comparison with the

Table 6. CLOUDY models for the three quasars: (1) $U = \frac{Q(H)}{4\pi r^2 n c}$ where $Q(H)$ is the number of hydrogen ionizing photons, r is the distance of the gas to the continuum source, n is the gas number density and c the speed of light.

Parameter	PG 1001+054	PG 2112+059	PG 1535+547
N_{H} [cm^{-2}]	$10^{23.3}$	$10^{22.8}$	$10^{22.5}$
$U^{(1)}$	$10^{2.7}$	$10^{1.7}$	$10^{1.8}$
α_{OX}	-1.72	-1.63	-1.72
α_{UV}	-0.5	-0.5	-0.5
α_{X}	-0.95	-0.95	-0.95

warm absorbers recently detected in other quasars of similar luminosity is not possible because Porquet et al. (2004) could not make a detailed analysis due to the lack of signal to noise of the spectra and Piconcelli et al. (2004b) were able to do such an analysis for only four quasars, two of them soft X-ray weak. Although not statistically significant, it is interesting to note that the two soft X-ray weak quasars show higher N_{H} and ξ than the two “normal” quasars, which have $N_{\text{H}} \sim 10^{22} \text{ cm}^2$ and $\xi \sim 40\text{--}90 \text{ erg cm}^{-1} \text{ s}^{-1}$, both lower values than those found in the three quasars discussed here.

6.2. Optical-UV-X-ray SED

After correcting for intrinsic absorption in PG 1535+547, it is remarkable that roughly the same incident spectral shape works for the three objects, and that only the column density and ionization parameters make the difference in the X-ray spectra. Given the observed flux of the sources and the estimates of the ionization parameters and spectral shape from the CLOUDY models, the only undefined quantity is nr^2 . Unfortunately, the location and density of the absorber are weakly constrained by photoionization models and we cannot discriminate between a low density ($n < 10^2 \text{ cm}^{-3}$) absorber in the interstellar medium of the host galaxy ($r \geq 1 \text{ kpc}$) or a high density material ($n \sim 10^6, 10^9, 10^{11} \text{ cm}^{-3}$) inside the nuclear region with $r \sim 10 \text{ pc}, 1 \text{ pc}, 20 \text{ lt.d.}$ The latter is a typical distance-density combination for the BLR clouds in nearby Seyfert 1 galaxies. However, the ionization parameters in Fig. 6 are significantly larger than the typical BLR values ($\xi \leq 10^{-1} \text{ erg cm}^{-1} \text{ s}^{-1}$). This means that the ionized absorber is different from the material responsible for the broad UV emission lines, consistent with our CLOUDY results that no significant UV emission is expected from the absorbing material (Sect. 5 and Fig. 11). The former solution is reminiscent of the molecular torus postulated by unification schemes, both in terms of distances ($1 < d < 10 \text{ pc}$) and densities ($10^6 < n < 10^9 \text{ cm}^{-3}$). The ionization parameter is however very different. We speculate that the warm absorber in X-Ray weak quasars could originate in material boiled off the torus inner wall by the intense nuclear radiation field. In such case, X-ray weak quasars would be normal quasars seen at a special angle such that our line of sight to the nucleus grazes the upper tip of the torus. An alternative possibility is that the torus is lacking in X-ray weak quasars, being replaced by a high ionization screen transparent to UV

and optical photons. This would explain the deficit of “type 2” quasars in existing surveys.

6.3. Variability of PG 2112+059

PG 2112+059 shows significant X-ray variability (Gallagher et al. 2004). In comparison with the September 2002 Chandra observation, our data from May 2003 show a factor 6.7 increase of the 0.5–2.0 keV flux and a factor 2.1 increase in the 2–7 keV band. Our fluxes remain nevertheless lower than those measured with ASCA in November 1999 by factors 0.66 and 0.47, respectively. The larger variability amplitude in the soft X-ray band is consistent with the ionized absorber model: as the flux increases, the absorbing material gets more ionized and its opacity in the soft X-ray decreases.

6.4. Broad Fe K_{α} line

The spectrum of PG 2112+059 obtained by Chandra in September 2002, required a broad iron K_{α} fluorescence emission line (Gallagher et al. 2004).

A line as observed by Chandra is detected in the XMM-Newton data at the $\sim 98\%$ confidence level only. Interestingly, the equivalent width is about half the equivalent width obtained for the Chandra observation which has to be compared with a factor of ~ 2.1 increase of the continuum flux in the 2.0–7.0 keV energy band. Therefore, the two observations are consistent with continuum variation while the flux of the iron line remains constant.

The XMM-Newton spectra of PG 1535+547 statistically require a broad iron line, whereas the line was absent from 1999 ASCA data. This points toward a variable emission line.

Given that broad Fe K_{α} fluorescence emission lines are only rarely seen in Chandra or XMM-Newton observations of AGNs, it is quite remarkable that two of the three quasars studied here show a variable broad Fe K_{α} fluorescence emission line. Although the number of studied objects is far too small to draw definitive conclusions, we should consider that variable broad Fe K_{α} fluorescence emission lines might be a second characteristic of X-ray weak quasars in general. This would then suggest exceptional physical parameters or viewing angles as proposed by Brandt et al. (2000).

7. Conclusions

1. All three objects show an ionized absorber characterized by high column densities and high ionization parameters, which explain their X-ray weakness. In combination with the similar results of Brinkmann et al. (2004) for two other X-ray weak quasars, it seems likely that such absorbers are characteristic of X-ray weak quasars in general. They are different from the warm absorbers found commonly in AGNs (if warm absorbers found by Porquet et al. (2004) and Piconcelli et al. (2004b) have similar properties as Seyfert 1 warm absorbers), which show much lower column densities and ionization parameters.

2. Using the observed SED and the material properties as inferred from the fits to the X-ray spectra as input for CLOUDY photoionization code, we have demonstrated that strong X-ray absorption and a few weak X-ray emission features are indeed expected from high ionization and high column densities material in the line of sight to the quasar. No UV emission, nor absorption features are expected, consistent with too high an ionization parameter compared with typical BLR values. We speculate on a possible relationship between this high column density absorbing material and the obscuring material that blocks the AGN light in high luminosity type 2 objects. The high ionization degree of the obscuring material in the soft X-ray weak quasars studied here makes the material almost transparent for UV-optical wavelengths in spite of the high column density. Our data do not allow to test this hypothesis further.
3. PG 1535+547 shows a variable broad Fe K_{α} fluorescence emission line, similar to the one detected in the Chandra observation of PG 2112+059 reported by Gallagher et al. (2004). Given that broad Fe K_{α} fluorescence emission lines have been rarely detected with XMM-Newton and Chandra and that only five X-ray weak quasar are well studied so far, a variable broad Fe K_{α} fluorescence emission lines might also be typical of X-ray weak quasars.

Acknowledgements. This research has made use of the NASA/IPAC Extragalactic Database (NED) which is operated by the Jet Propulsion Laboratory, California Institute of Technology, under contract with the National Aeronautics and Space Administration.

References

- Alonso-Herrero, A., Quillen, A. C., Simpson, C., et al. 2001, *AJ*, 121, 1369
- Anders, E., & Grevesse, N. 1989, *Geochim. Cosmochim. Acta*, 53, 197
- Arnaud, K. 1996, *ADASS*, 5, 17
- Avni, Y., & Tananbaum, H. 1982, *ApJ*, 262, L17
- Avni, Y. 1976, *ApJ*, 210, 642
- Balucinska-Church, M., & McCammon, D. 1992, *ApJ*, 400, 699
- Boroson, T. A., & Green, R. F. 1992, *ApJS*, 80, 109
- Brandt, W. N., Laor, A., & Wills, B. J. 2000, *ApJ*, 528, 637
- Brinkmann, W., Papadakis, I. E., & Ferrero, E. 2004, *A&A*, 414, 107
- Calzetti, D., Armus, L., Bohlin, R. C., et al. 2000, *ApJ*, 533, 682
- Cardelli, J. A., Clayton, G. C., & Mathis, J. S. 1989, *ApJ*, 345, 245
- Dickey, J. M., & Lockman, F. J. 1990, *ARA&A*, 28, 215
- Done, C., Mulchaey, J. S., Mushotzky, R. F., et al. 1992, *ApJ*, 395, 275
- Elvis, M., & Fabbiano 1984, *ApJ*, 280, 91
- Elvis, M., Wilkes, B. J., & Lockman, F. J. 1998, *ApJ*, 97, 777
- Gallagher, S. C., Brandt, W. N., & Laor, A. 2001, *ApJ*, 546, 795
- Gallagher, S. C., Brandt, W. N., Wills, B. J., et al. 2004, *ApJ*, 603, 425
- Green, R. F. 1979, *PASP*, 88, 665
- Green, P. J., & Mathur, S. 1996, *ApJ*, 462, 637
- Jannuzi, B. T., Bahcall, J. N., Bergeron, J., et al. 1998, *ApJS*, 118, 1
- Jansen, F., Lumb, D., Altieri, B., et al. 2001, *A&A*, 365, L1
- Kendall, M. G., & Stuart, A., *The advanced Theory of Statistics Vol. 2* (New York: Hafner), Sect. 19.26, 97
- Kirsch, M. 2003, EPIC status of calibration and data analysis, http://xmm.vilspa.esa.es/external/xmm_sw_cal/calib/index.shtml
- Laor, A., Fiore, F., Elvis, M., et al. 1997, *ApJ*, 477, 93
- Laor, A. 1991, *ApJ*, 376, 90
- Lockman, F. J., & Savage, B. D. 1995, *ApJS*, 97, 1
- Loiseau, N. ed. 2004 XMM-Newton Science Analysis System Users' Guide, V3.0, http://xmm.vilspa.esa.es/external/xmm_user_support/documentation/sas_usg/USG/index.html
- Mason, K. O., Breeveld, A., Much, R., et al. 2001, *A&A*, 365, 36
- Murphy, E. M., Lockman, F. J., & Laor, A. 1996, *ApJS*, 105, 369
- Phillips, M. M. 1978, *ApJS*, 38, 187
- Piconcelli, E., Jimenez-Bailón, E., Guainazzi, M., et al. 2004a, *MNRAS*, 351, 161
- Piconcelli, E., Jimenez-Bailón, E., Guainazzi, M., et al. 2004b, *A&A*, submitted
- Porquet, D., Reeves, J. N., O'Brien, P., et al. 2004, *A&A*, 422, 85
- Reynolds, C. S. 1997, *MNRAS*, 286, 513
- Schmidt, M., & Green, R. F. 1983, *ApJ*, 269, 353
- Smith, P. S., Schmidt, G. D., Allen, R. G., et al. 1997, *ApJ*, 488, 202
- Strüder, L., Briel, U., Dennerl, K., et al. 2001, *A&A*, 365, L18
- Turner, M. J. L., Abbey, A., Arnaud, M., et al. 2001, *A&A*, 365, L27
- Véron-Cetty, M.-P., Véron, P., & Gonçalves, A. C., et al. 1992, *A&A*, 372, 730
- Véron-Cetty, M.-P., & Véron, P. 2000, *A Catalogue Of Quasars And Active Galactic Nuclei*, 9th edition, ESO Scientific Report, 19, European Souther Observatory (München: Garching)
- Wang, T., Brinkmann, W., & Bergeron, J. 1996, *A&A*, 309, 81
- Wang, T. G., Brinkmann, W., Yuan, W., et al. 2000, *ApJ*, 545, 77
- Wills, B. J., Shang, Z., & Yuan, J. M. 2000, *New Astron. Rev.*, 44, 511
- Yan, M., Sadeghpour, H. R., & Dalgarno, A. 1998, *ApJ*, 496, 1044